

See discussions, stats, and author profiles for this publication at: <https://www.researchgate.net/publication/349306832>

# Temperature, differential-pressure and porosity inversion for ultra-deep carbonate reservoirs based on 3D rock physics templates

Article in *Geophysics* · February 2021

DOI: 10.1190/geo2020-0550.1

CITATIONS

10

READS

169

6 authors, including:



Jing Ba

Hohai University

196 PUBLICATIONS 2,351 CITATIONS

[SEE PROFILE](#)



José M Carcione

OGS Istituto Nazionale di Oceanografia e di Geofisica Sperimentale

631 PUBLICATIONS 14,020 CITATIONS

[SEE PROFILE](#)



Li-Yun Fu

China University of Petroleum

344 PUBLICATIONS 2,392 CITATIONS

[SEE PROFILE](#)



Mengqiang Pang

Hohai University

24 PUBLICATIONS 147 CITATIONS

[SEE PROFILE](#)

Some of the authors of this publication are also working on these related projects:



MT anisotropic inversion [View project](#)



Wave dispersion and attenuation [View project](#)

# Temperature, differential pressure, and porosity inversion for ultradeep carbonate reservoirs based on 3D rock-physics templates

Yijun Wei<sup>1</sup>, Jing Ba<sup>1</sup>, José M. Carcione<sup>2</sup>, Li-Yun Fu<sup>3</sup>, Mengqiang Pang<sup>1</sup>, and Hui Qi<sup>1</sup>

## ABSTRACT

Ultradeep carbonate reservoirs have high temperatures and pressures, complex pressure/tectonic stress settings, and complex pore structures. These conditions make their seismic detection and characterization difficult, particularly if the signal-to-noise ratio is low, as is the case in most situations. Moreover, the high risk of deep-drilling exploration makes it impractical to carry out normal logging operations. We have developed a temperature-differential pressure-porosity (TPP) rock-physics model based on the Biot-Rayleigh poroelasticity theory to describe the wave response of the reservoir. A preliminary analysis indicates that temperature, pressure, and porosity are well correlated with wave velocity and attenuation. On the basis of this theory, we have built 3D rock-physics templates that account for the effects of TPP on the P-wave impedance,  $V_P/V_S$  ratio, and attenuation. The templates are calibrated with laboratory, well-log, and seismic data of the S area (Shuntuoguole uplift, Tarim Basin, Xinjiang, China). Then, the template is used to obtain the properties of the reservoir at seismic frequencies. The predicted results are consistent with the field reports (high temperature, low differential pressure, and high porosity) indicating high production rates. The methodology will be useful for hydrocarbon exploration in ultradeep carbonate reservoirs.

## INTRODUCTION

With the decline of shallow petroleum discoveries, the exploration prospects are gradually moving from medium-deep to ultradeep layers, as is the case of unconventional oil-gas resources around the

world (Pang et al., 2015; Guo et al., 2019). An ultradeep carbonate reservoir in China is the S area of the Tarim Basin, Xinjiang, where the Ordovician limestone is rich in oil and gas resources (Qi, 2016; Wan et al., 2017; Jiao, 2018; Ding et al., 2020). Temperature and pressure affect the distribution of hydrocarbons, and porosity and cracks are important factors controlling their migration and accumulation. Temperature is a good fluid indicator for ultradeep carbonate fault-karst reservoirs (Lei et al., 2020). Compared to shallow reservoirs, ultradeep reservoirs generally exhibit higher temperatures and a complex pressure setting and pore network, so the use of conventional rock-physics models may not be appropriate (Yao et al., 2018; Gu et al., 2019; Tian et al., 2019).

Jaya et al. (2010) analyze the effects of temperature on seismic wave velocity and attenuation by using a modified Gassmann equation and show that the fluid properties are important. P-wave velocity decreases with increasing temperatures and attenuation increases due to the formation of bubbles and microfractures. Batzle et al. (2006) find that the P- and S-wave velocities of dry samples do not depend on temperature and that the S-wave velocity increases with the increasing fluid viscosity. The effect of differential pressure (confining minus pore) is considered in many works (Liu et al., 1998; Pham et al., 2008; Pimienta et al., 2015, 2016; Chapman et al., 2016, 2017). The results show that the wave velocity increases and attenuation decreases with differential pressure, effects dictated by the microstructure of the rock. Agersborg et al. (2009) consider the effects of pore geometry on the P- and S-wave properties. Kern et al. (2001) conduct experiments on ultradeep reservoir cores to study the effect of temperature and pressure on velocity. They find a nonlinear and a linear trend at low and high confining pressures, respectively, and they find a linear decrease at high pressures and temperatures. The effects of cracks are significant, and their characteristics can be obtained from the elastic-moduli dependence on pressure (Cheng and Toksöz, 1979; Tran et al., 2008; Cheng et al., 2020). Smith et al. (2010) study the effects of confining pressure and pore structure on

Manuscript received by the Editor 28 July 2020; revised manuscript received 27 January 2021; published ahead of production 14 February 2021; published online 21 April 2021.

<sup>1</sup>Hohai University, School of Earth Sciences and Engineering, Nanjing 211100, China. E-mail: jingba@188.com (corresponding author).

<sup>2</sup>Hohai University, School of Earth Sciences and Engineering, Nanjing 211100, China and National Institute of Oceanography and Applied Geophysics — OGS, Trieste 34010, Italy.

<sup>3</sup>China University of Petroleum (East China), Key Laboratory of Deep Oil and Gas, Qingdao 266580, China.

© 2021 Society of Exploration Geophysicists. All rights reserved.

the wave velocity at ultrasonic frequencies and find that there is no appreciable change in stiff (equant) porosity with the increasing confining pressure. The observed increase in P-wave velocity can only be ascribed to the closure of compliant (soft) pores.

Differential-medium theories are used to relate elastic properties to the microstructure (Walsh, 1965; Mori and Tanaka, 1973; Kuster and Toksöz, 1974). David and Zimmerman (2012) extend the Zimmerman (1991) method, based on the Mori and Tanaka (1973) theory, to obtain the distribution of crack aspect ratios from the dry-rock velocity. Batzle and Wang (1992) establish the pressure and temperature dependencies of pore fluids. The Biot-Gassmann theory (Gassmann, 1951; Biot, 1962) is often used for fluid substitution, but Gregory (1976) finds inconsistencies due to the fact that it is a low-frequency limit and ignores local fluid effects that induce wave dispersion and attenuation (Murphy, 1984). Pride et al. (2004) describe wave propagation in patchy-saturated rocks with a double-porosity theory, and Ba et al. (2011, 2012, 2017) consider mesoscopic fluid-flow effects and derive wave-propagation equations for a heterogeneous porous medium to model attenuation at different frequency bands.

Most research on formation-pressure prediction is based on the compaction effect and has been applied in conventional shale formations (Hottman and Johnson, 1965; Eaton, 1972). However, due to the complexity of carbonate rocks, the compaction effect is not evident. Fillippone (1979) combines the formation velocity with log and seismic data to develop a formation-pressure prediction model independent of the compaction trend. The principle of effective stress proposed by Terzaghi (1943) is an important theoretical basis for the prediction of formation pressure in carbonate reservoirs. Xia et al. (2005) use log data to predict the pore pressure of carbonate reservoirs at eight wells, based on the principle of effective stress. Cheng et al. (2013) use the effective-stress principle combined with ultrasonic experiments to establish a new pore-pressure prediction model suitable for carbonates. Liu et al. (2020) predict the temperature in deep and ultradeep strata and find that the spatial distribu-

tions are mainly controlled by the basement structural pattern. The temperature ranges at 6, 7, and 8 km depths are 118°C–172°C, 136°C–198°C, and 190°C–224°C, respectively. Rock-physics templates (RPTs) are a useful tool for lithology and pore fluid interpretation, based on well-log data and elastic inversion (Odegaard and Avseth, 2004). Ba et al. (2013) build multiscale RPTs based on the Biot-Rayleigh theory to predict the porosity and saturation of carbonate gas reservoirs. Li et al. (2019) use 3D RPTs based on the effective-medium theory and Gassmann equations to predict theoretical porosity, pore aspect ratio, and fluid saturation in carbonates.

Here, we establish the relation between the dry-rock moduli and the micropore structure at different differential pressures and temperatures, based on the Mori-Tanaka theory, and the fluid properties are obtained with the Batzle-Wang equations. Then, we develop the temperature-differential pressure-porosity (TPP) rock-physics model based on the Biot-Rayleigh theory (Ba et al., 2011) and 3D RPTs, which are calibrated with ultrasonic, log, and seismic data from the S area of the Tarim Basin, Xinjiang, China. The templates are then used to predict the TPP of the area.

## ROCK-PHYSICS MODEL

Ultradeep carbonate reservoirs, such as the Shuntuoguole uplift of the Tarim Basin (S area), have depths greater than 7 km, temperatures exceeding 150°C, and a complex formation system with pressures greater than 60 MPa. The flowchart is shown in Figure 1. The target reservoir rocks are mainly limestones with high calcite content and a small amount of dolomite, and we use the Voigt-Reuss-Hill average to estimate the grain elastic moduli. We consider stiff pores and compliant cracks, which have spherical and oblate shapes, and we use the Mori-Tanaka theory to analyze the effects of temperature and pressure on the moduli and pore structure. The Batzle and Wang (1992) equations provide the properties of fluids. Finally, we use the Biot-Rayleigh theory (Ba et al., 2011) to obtain the wave velocities and attenuation of the oil-saturated rocks at different frequency bands.

### Mineral stiffness moduli

The reservoir of this study is a limestone, dominantly calcite, with a small amount of dolomite. The Voigt-Reuss-Hill average (Voigt, 1910; Reuss, 1929; Hill, 1952) is used to calculate the elastic modulus of the composite mineral:

$$K_s = \frac{1}{2} \left( \sum_{i=1}^N f_i K_i + 1 / \sum_{i=1}^N \frac{f_i}{K_i} \right), \quad (1)$$

$$G_s = \frac{1}{2} \left( \sum_{i=1}^N f_i G_i + 1 / \sum_{i=1}^N \frac{f_i}{G_i} \right), \quad (2)$$

where  $K_s$  and  $G_s$  are the bulk and shear moduli of the grains, respectively;  $f_i$ ,  $K_i$ , and  $G_i$  represent the volume ratio, and bulk and shear moduli of mineral  $i$ , respectively; and  $N$  is the number of minerals.

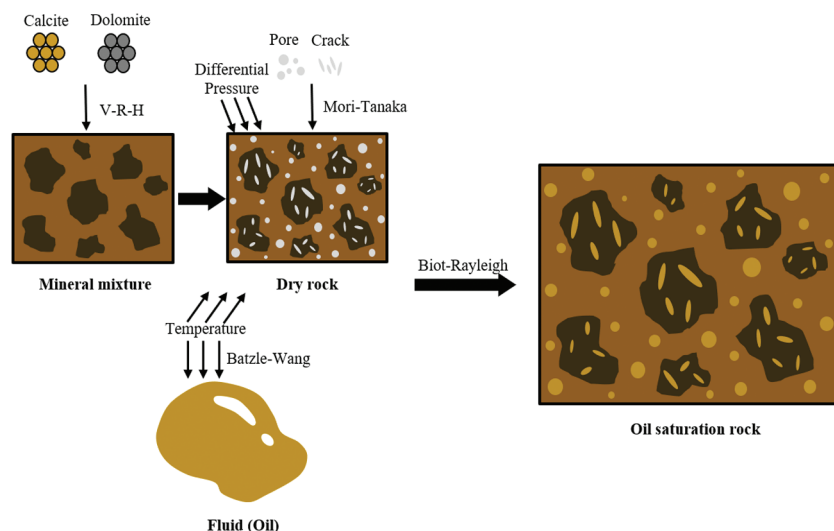


Figure 1. Flowchart of the ultradeep carbonate rock-physics modeling. We use the Voigt-Reuss-Hill average and the Mori-Tanaka theory to estimate the grain and dry-rock elastic moduli, respectively. The Batzle and Wang equations provide the properties of the fluids, and the wave velocities and attenuation of the oil-saturated rocks are obtained with the Biot-Rayleigh theory.

## Dry-rock moduli

Because the reservoir is buried below 7 km, the pore structure is greatly affected by temperature and differential pressure. There are many combinations of pore volumes and shapes. A simple method is to consider two void spaces and use the effective medium theory (Duran et al., 2019). We consider stiff pores and compliant cracks (Ruiz and Cheng, 2010). The bulk and shear moduli without cracks are given by (Mori and Tanaka, 1973)

$$K_{\text{stiff}} = K_s / \left( 1 + \frac{\phi_{\text{stiff}}}{1 - \phi_{\text{stiff}}} P(\alpha_{\text{stiff}}, v_s) \right), \quad (3)$$

$$G_{\text{stiff}} = G_s / \left( 1 + \frac{\phi_{\text{stiff}}}{1 - \phi_{\text{stiff}}} Q(\alpha_{\text{stiff}}, v_s) \right), \quad (4)$$

where  $\phi_{\text{stiff}}$  is the stiff porosity and  $P$  and  $Q$  are the shape factors (see Appendix A).

When the cracks are completely closed under high differential pressures, only the stiff pores are present and the stiff porosity can be estimated. The corresponding bulk and shear moduli,  $K^{\text{hp}}$  and  $G^{\text{hp}}$ , respectively, are obtained from the P- and S-wave velocities as

$$K^{\text{hp}} = \rho \left( (V_p^{\text{hp}})^2 - \frac{4}{3} (V_s^{\text{hp}})^2 \right), \quad (5)$$

$$G^{\text{hp}} = \rho (V_s^{\text{hp}})^2, \quad (6)$$

where the superscript ‘‘hp’’ denotes the high differential pressure and  $\rho$  is the mass density. Combining equations 3–6, the aspect ratio of the stiff pores  $\alpha_{\text{stiff}}$  is obtained by a least-squares algorithm applied to these moduli.

The effective dry-rock bulk and shear moduli with cracks are (Mori and Tanaka, 1973), respectively,

$$K_{\text{eff}} = K_{\text{stiff}} / \left( 1 + \frac{16(1 - (v_{\text{stiff}})^2)\Gamma}{9(1 - 2v_{\text{stiff}})} \right), \quad (7)$$

$$G_{\text{eff}} = G_{\text{stiff}} / \left( 1 + \frac{32(1 - v_{\text{stiff}})(5 - v_{\text{stiff}})\Gamma}{45(2 - v_{\text{stiff}})} \right), \quad (8)$$

where  $v_{\text{stiff}} = (3K_{\text{stiff}} - 2G_{\text{stiff}})/(6K_{\text{stiff}} + 2G_{\text{stiff}})$  is the Poisson’s ratio of the stiff pores and  $\Gamma$  is the crack density.

The temperature and pressure dependence of the effective moduli are closely related to the crack density (Sarout et al., 2017; Wei et al., 2020). When this is specified, the elastic moduli can be obtained from equations 7 and 8, and vice versa. The elastic modulus at different temperatures and pressures can be obtained from the wave velocities. Then, the crack density at each temperature and differential pressure  $\Gamma(T, p)$  can be computed by least-squares regression based on the elastic moduli.

The relation between the pore aspect ratio and the differential pressure is (Zhang et al., 2019)

$$\alpha_p = \frac{4[1 - (v_{\text{eff}})^2]p}{\pi E_{\text{eff}}}, \quad (9)$$

where  $E_{\text{eff}}$  is the effective Young modulus, defined as  $E_{\text{eff}} = 3K_{\text{eff}}[1 - 2v_{\text{eff}}]$ .

The relation between crack porosity and crack density is (David and Zimmerman, 2012)

$$\phi_2 = \frac{4\pi\alpha_p}{3} \Gamma_p. \quad (10)$$

## Equation of motion and dispersion equation

Because the temperature in the study area is greater than 150°C, the fluid modulus ( $k_f$ ), viscosity ( $\eta$ ), and density ( $\rho_f$ ) are highly affected, which can be estimated by the Batzle and Wang (1992) equations under variable temperatures (see Appendix B). We use the Biot-Rayleigh equations (Ba et al., 2011) to obtain the properties of the saturated rock,

$$\begin{aligned} N\nabla^2 \mathbf{u} + (A + N)\nabla \varepsilon + Q_1 \nabla(\zeta^{(1)} + \phi_2 \varsigma) + Q_2 \nabla(\zeta^{(2)} - \phi_1 \varsigma) \\ = \rho_{11} \ddot{\mathbf{u}} + \rho_{12} \ddot{\mathbf{U}}^{(1)} + \rho_{13} \ddot{\mathbf{U}}^{(2)} + b_1(\dot{\mathbf{u}} - \dot{\mathbf{U}}^{(1)}) + b_2(\dot{\mathbf{u}} - \dot{\mathbf{U}}^{(2)}), \end{aligned} \quad (11a)$$

$$Q_1 \nabla \varepsilon + R_1 \nabla(\zeta^{(1)} + \phi_2 \varsigma) = \rho_{12} \ddot{\mathbf{u}} + \rho_{22} \ddot{\mathbf{U}}^{(1)} - b_1(\dot{\mathbf{u}} - \dot{\mathbf{U}}^{(1)}), \quad (11b)$$

$$Q_2 \nabla \varepsilon + R_2 \nabla(\zeta^{(2)} - \phi_1 \varsigma) = \rho_{13} \ddot{\mathbf{u}} + \rho_{33} \ddot{\mathbf{U}}^{(2)} - b_2(\dot{\mathbf{u}} - \dot{\mathbf{U}}^{(2)}), \quad (11c)$$

$$\begin{aligned} \phi_2 \left( Q_1 \varepsilon + R_1(\zeta^{(1)} + \phi_2 \varsigma) \right) - \phi_1 \left( Q_2 \varepsilon + R_2(\zeta^{(2)} - \phi_1 \varsigma) \right) \\ = \frac{1}{3} \rho_f \zeta R_{12}^2 \frac{\phi_1^2 \phi_2 \phi_{20}}{\phi_{10}} + \frac{1}{3} \frac{\eta \phi_1^2 \phi_2 \phi_{20}}{\kappa_1} \zeta R_{12}^2, \end{aligned} \quad (11d)$$

where  $\mathbf{u}$ ,  $\mathbf{U}^{(1)}$ , and  $\mathbf{U}^{(2)}$  are the displacement vectors of the solid, fluid phase 1 (fluid in stiff pores), and fluid phase 2 (fluid in microcracks), respectively;  $\varepsilon$ ,  $\zeta^{(1)}$ , and  $\zeta^{(2)}$  are the variations of fluid contents;  $\varsigma$  is the fluid increment caused by the local flow process;  $\phi_{10}$  and  $\phi_{20}$  are the local porosities of the main skeleton (only stiff pores) and crack;  $\phi_1 = v_1 \phi_{10}$  and  $\phi_2 = v_2 \phi_{20}$  are the absolute porosities of the two types of pores;  $v_1$  and  $v_2$  are the corresponding volume ratios;  $R_{12}$  is the radius of the microcrack;  $b_1$  and  $b_2$  are the Biot dissipation coefficients related to the absolute porosities  $\phi_1$  and  $\phi_2$  and permeabilities  $\kappa_1$  and  $\kappa_2$  of the main skeleton and crack, respectively;  $\rho_{11}$ ,  $\rho_{12}$ ,  $\rho_{13}$ ,  $\rho_{22}$ , and  $\rho_{33}$  are the density components; and  $A$ ,  $N$ ,  $Q_1$ ,  $Q_2$ ,  $R_1$ , and  $R_2$  are the stiffness coefficients (see Appendix C). Substituting a plane-wave kernel into equation 11, we obtain the P- and S-wave complex wavenumbers (see Appendix D),  $V_P$  and  $V_S$ , respectively, of the wet rock (Ba et al., 2011).



## APPLICATION OF THE MODEL

### Geologic setting

The study area is located in the S area, Shuntuoguole uplift, Tarim Basin, Xinjiang, China. The Ordovician carbonate fault-karst reservoirs are currently the main exploration horizon of this area, which is composed of the Yijianfang and Yingshan Formations. Karst caves, pores, and microcracks caused by multistage strike-slip faulting and dissolution develop in the reservoirs. The complex interconnectivity generates the complexity of the fluid flow dynamic with potential geothermal sources. The Lower-Cambrian hot-alkaline brine may be the heat source, and strike-slip faulting provides channels for hydrothermal fluid upwellings (Liu et al., 2020).

### Carbonate samples

The rock samples and data are from the deep-carbonate S area. As shown in Figure 2, a thin section of a limestone sample contains multiple microcracks with different apertures in the range of 0.01–0.03 mm, and the surface porosity is less than 1%.

The ultrasonic experiment consists of a digital oscilloscope (Tektronix TDS 420 A) and a pulse generator (Panametrics 5077PR) (Guo et al., 2009). The measuring system has independent temperature and pressure (pore and confining) control units. The limestone sample is saturated with oil by means of the vacuum and pressure saturation method and placed on a rubber jacket. The porosity (with rare clay and dissolved intergranular pores) is 2.5%, the permeability is 0.023 mD, and the dry-rock density is 2.66 g/cm<sup>3</sup>. Differential pressures (confining minus pore) of 15, 20, 25, 30, 40, 50, 60, and 70 MPa are applied up to 140°C and maintained for 30 min by heating the fluid with a wire within the high-pressure vessel. A stress-temperature path sketch is shown in Figure 3. The ultrasonic pulse transmission method is used to obtain the waveform at each differential pressure, and velocities are computed from the first arrival. The P-wave quality factor  $Q$  is obtained with the spectral-ratio method using an aluminum rod as a reference (Toksöz et al., 1979; Pang et al., 2020), and then the so-called P-wave dissipation factor is  $1/Q$ .

The sonic-log data are selected from oil well B of the S area, which is located in the northern margin of the Shuntuoguole low

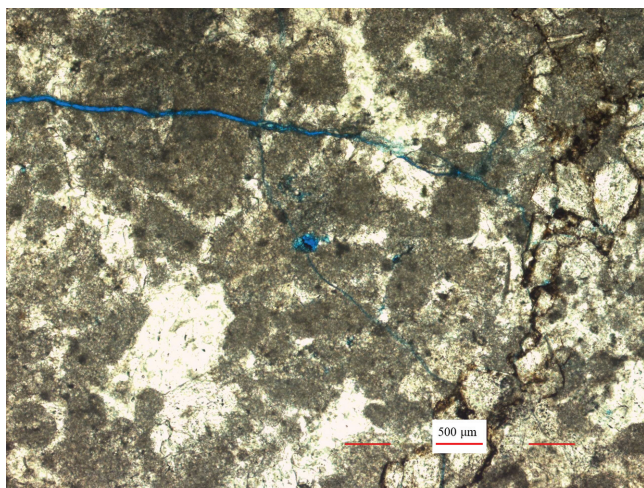


Figure 2. Thin section of a limestone sample containing multiple microcracks with different apertures.

uplift. The completion horizon is the Yingshan Formation, and the drilling depth is 7647 m. The terms  $V_p$  and  $V_p/V_s$  are extracted from the seismic traces at the borehole location after a three-term inversion by using prestack angle gathers (Aki and Richards, 1980). The porosity for seismic data calibration is obtained from the log data and the traces around the well. To extract the attenuation from the seismic data, a time-frequency analysis is first used to obtain the amplitude spectrum based on the generalized S transform. Then, the layer with a higher centroid frequency is selected as a reference. Comparing the reference spectrum with those of the other layers, the dissipation factor (inverse of  $Q$ ) is obtained by the improved frequency-shift method (Tu and Lu, 2009; Pang et al., 2019, 2020):

$$Q = \frac{\sqrt{\pi^5} t f_{c1} f_{c0}^2}{16(f_{c0}^2 - f_{c1}^2)}, \quad (12)$$

where  $t$  is the propagation time and  $f_{c0}$  and  $f_{c1}$  are the centroid frequencies of the signal before and after propagation, respectively.

There is the problem of uncertainty in attenuation estimation. To obtain  $1/Q$ , Quan and Harris (1997) propose a centroid-frequency-shift method, in which the systematic errors increase with attenuation. Zhang and Ulrych (2002) present a peak-frequency-shift method, which is more accurate, but it is unstable due to the noise. Tu and Lu (2009) compare the two methods and propose an improved version, which we use in this study. Their results show that the error range is 0.2%–4.06% and the standard deviation range between the estimated and true  $Q$ s is 0.05–2.12. Although the attenuation estimation suffers from uncertainty and deviations, the results are instructive and the general trend can effectively guide the seismic identification of in situ reservoir properties.

### Model analysis

The bulk modulus, shear modulus, and density of calcite are 63.7 GPa, 31.7 GPa, and 2700 kg/m<sup>3</sup>, and those of dolomite are 76.4 GPa, 49.7 GPa, and 2870 kg/m<sup>3</sup>, respectively (Mavko et al., 2009). Assuming that the volume ratio of calcite ( $f_1$ ) is 100%, 90%, 80%, 70%, and 60%, we obtain the curves shown in Figure 4. When

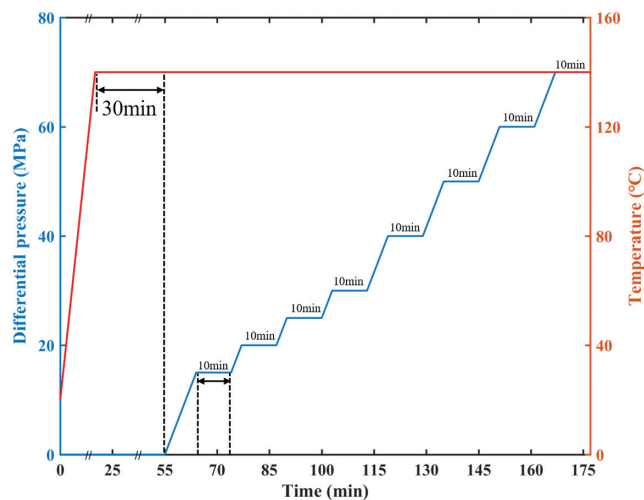


Figure 3. Stress-temperature path sketch. The blue and red lines refer to the differential pressure and temperature, respectively, under different times.

this ratio is 90%, the curve is in good agreement with the ultrasonic laboratory data. In this case, the bulk modulus, shear modulus, and density of the grains are 64.9 GPa, 33.2 GPa, and 2716 kg/m<sup>3</sup>, respectively.

We obtain the elastic moduli at dry and full saturation and in situ conditions, and we compare the results with Gassmann's equations (Gassmann, 1951). Figure 5 shows that the moduli depend on the differential pressure and that those estimated with the Biot-Rayleigh theory (Ba et al., 2011) are in good agreement with the ultrasonic data at full oil saturation, whereas the shear moduli estimated with the Biot-Rayleigh theory and Gassmann's equations are the same at dry and full-oil saturation conditions.

**Wave properties**

The rock-physics model described in the previous section is used to obtain the effects of TPP on the wave properties at different

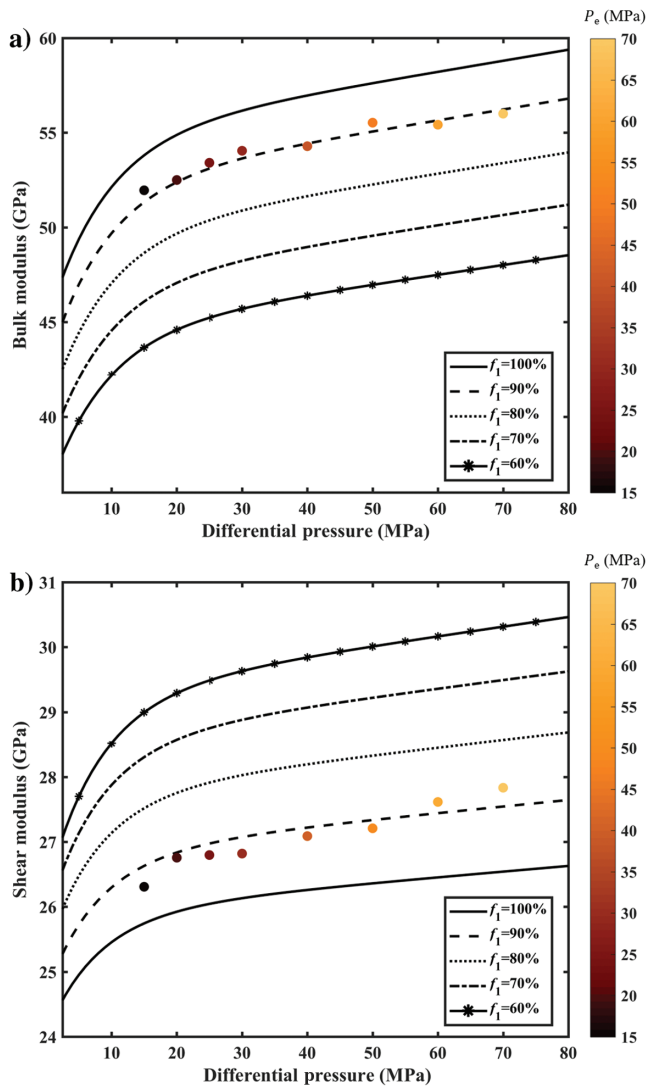


Figure 4. (a) Bulk and (b) shear moduli as a function of differential pressure. Different lines indicate different mineral contents. The circles are the ultrasonic laboratory data at different differential pressures (indicated by the color bar).

frequencies. We consider  $\phi_{20} = 0.6\%$ ,  $\kappa_2 = 0.1 \times 10^{-17} \text{ m}^2$ ,  $R_{12} = 2.8 \times 10^{-6} \text{ m}$ , and  $\kappa_1 = 1.11 \times 10^{-18} \text{ m}^2$ . Figure 6 shows the wave response at ultrasonic frequencies for TPP, where the porosity of the rock sample is 0.025 and the temperature is 140° C, with the colors corresponding to different differential pressures. In this case, the velocity agrees well and the attenuation has some discrepancies, which could be related to errors in processing or in the experimental measurements. Note that the P-wave velocity decreases and the attenuation increases with increasing temperature and porosity, whereas with the increasing pressure, the velocity gradually increases and the attenuation decreases. When the differential pressure is less than 40 MPa, the P-wave velocity increases more rapidly. At 80 MPa, the attenuation at the same porosity and different temperatures tends to be the same, and the smaller the porosity the weaker the effect of temperature on the attenuation is. This is mainly caused by the closure of microcracks at high differential pressures.

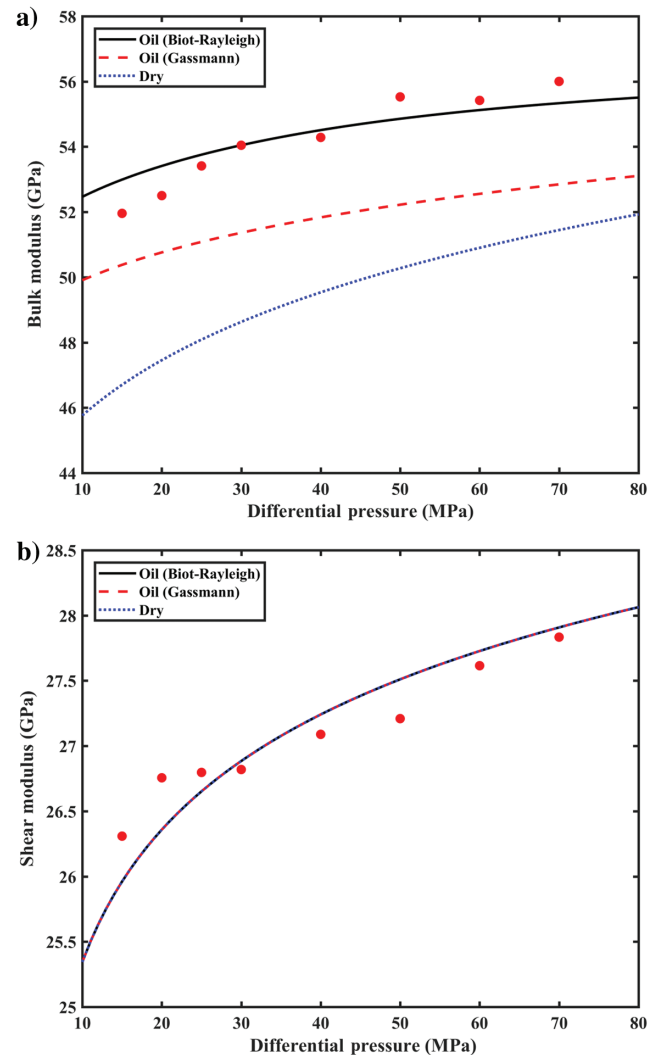


Figure 5. (a) Bulk and (b) shear moduli as a function of differential pressure. The solid black and dashed red lines represent the oil-saturated moduli obtained with the Biot-Rayleigh theory and Gassmann equation, respectively. The blue dotted line refers to the dry-rock moduli, whereas the circles are the ultrasonic laboratory data.

To illustrate the properties at sonic frequencies, we consider  $\phi_{20} = 1\%$ ,  $\kappa_2 = 0.1 \times 10^{-16} \text{ m}^2$ ,  $R_{12} = 7.5 \times 10^{-5} \text{ m}$ , and  $\kappa_1 = 1.11 \times 10^{-17} \text{ m}^2$ . The results, presented in Figure 7, show that increasing porosity or temperature and decreasing differential pressure imply decreasing velocity and increasing attenuation. However, the combined effect of pressure and temperature yields different outcomes; e.g., the velocity at 100 MPa and 180°C (the dashed line) is higher than that at 60 MPa and 160°C (the solid line).

Regarding the seismic frequency band, we consider  $\phi_{20} = 1\%$ ,  $\kappa_2 = 0.1 \times 10^{-15} \text{ m}^2$ ,  $R_{12} = 2.8 \times 10^{-3} \text{ m}$ , and  $\kappa_1 = 1.11 \times 10^{-16} \text{ m}^2$ . Figure 8 shows the results. As previously, the P-wave velocity decreases and attenuation increases with the increasing temperature and porosity and decreasing pressure. The standard deviation between the predicted and seismic P-wave velocity is 33.1848 m/s, and that of  $1/Q$  is 0.0045.

Because the classic 2D RPTs are unable to predict more than two parameters of the reservoir accurately, 3D RPTs are built to consider

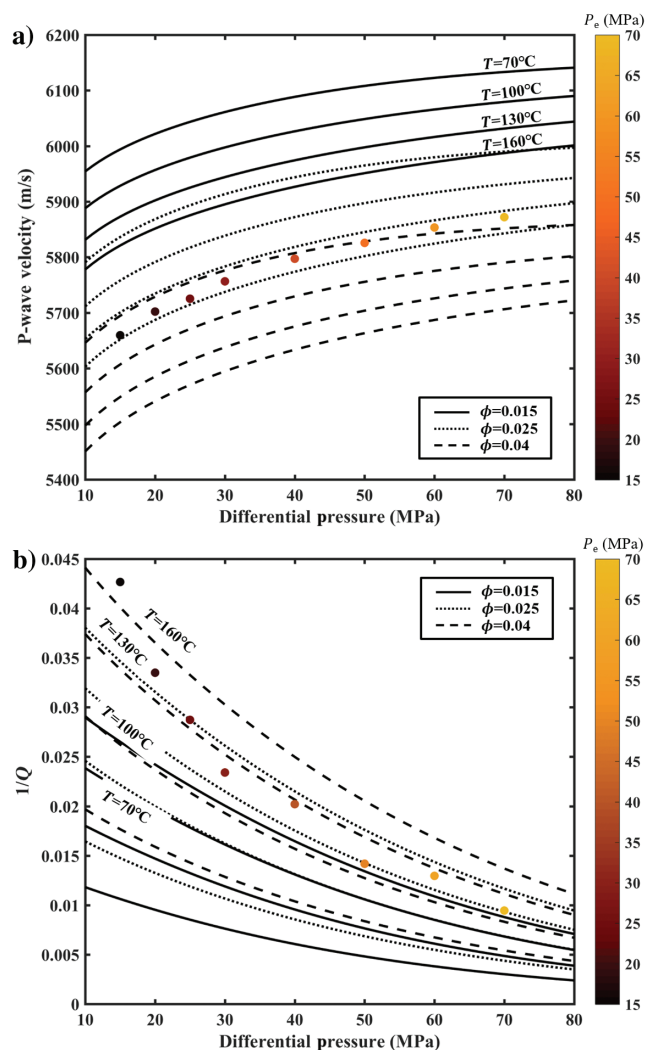


Figure 6. (a) The  $V_p$  and (b) dissipation factor as a function of differential pressure at ultrasonic frequencies. The temperatures are given. The dashed, dotted, and solid lines correspond to porosities of 0.04, 0.025, and 0.015, respectively. The circles are the ultrasonic laboratory data at different differential pressures (indicated by the color bar).

wave attenuation, P-wave impedance, and the P- to S-wave velocity ratio as a function of TPP.

## RPT AND CALIBRATION

### Ultrasonic frequencies

The P-wave impedance,  $V_p/V_s$  ratio, and attenuation of a 3D RPT at 1 MHz are shown in Figure 9a. The red, black, and blue isolines correspond to the TPP properties. The plot shows the expected behaviors, e.g., an increasing temperature, the  $V_p/V_s$  ratio and P-wave impedance decrease and attenuation increases as well as increasing differential pressure, and the  $V_p/V_s$  ratio and attenuation decrease and the P-wave impedance increases. The  $V_p/V_s$  ratio decreases and then increases with porosity. It can also be observed that the higher the pressure, the smaller the change in attenuation, which means that the influence of temperature and porosity on attenuation is smaller, which is consistent with the results shown in Figure 6b. Figure 9b shows a temperature-pressure template at a porosity of 2.5%, showing that the model agrees with the data (circles). For

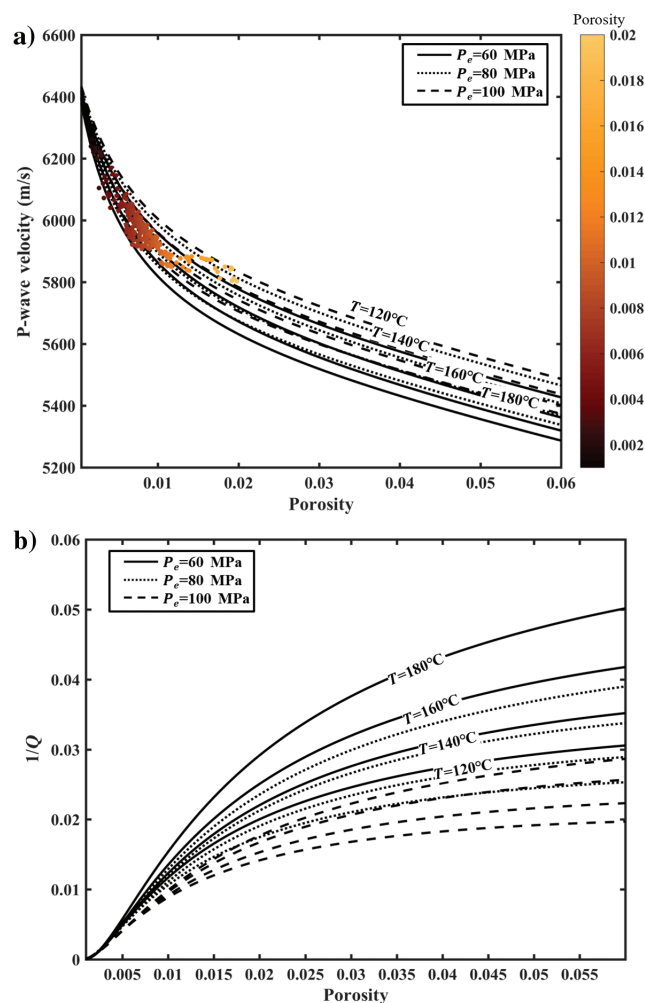


Figure 7. (a) The  $V_p$  and (b) dissipation factor as a function of porosity at sonic frequencies. The temperatures are given. The dashed, dotted, and solid lines correspond to differential pressures of 100, 80, and 60 MPa, respectively. The circles are the sonic log data at different porosities (indicated by the color bar).



constant porosity and temperature, the  $V_P/V_S$  ratio and P-wave impedance of the data increase and the attenuation decreases with pressure.

**Sonic frequencies**

Figure 10a shows the RPT at 1 kHz. In this case, there are no attenuation data and only P-wave impedance and  $V_P/V_S$  ratio are used for calibration (Figure 10b). The color bar in Figure 10b corresponds to the porosity of the log data. The porosity variation of the data is in good agreement with the distribution of the P-wave impedance and  $V_P/V_S$  ratio with porosity in the template. The P-wave impedance of the template and log data increase with decreasing porosity, whereas the  $V_P/V_S$  ratio decreases.

**Seismic frequencies**

Figure 11a and 11b shows the 3D RPT and the calibration at 30 Hz, respectively. The symbols in Figure 11b correspond to the

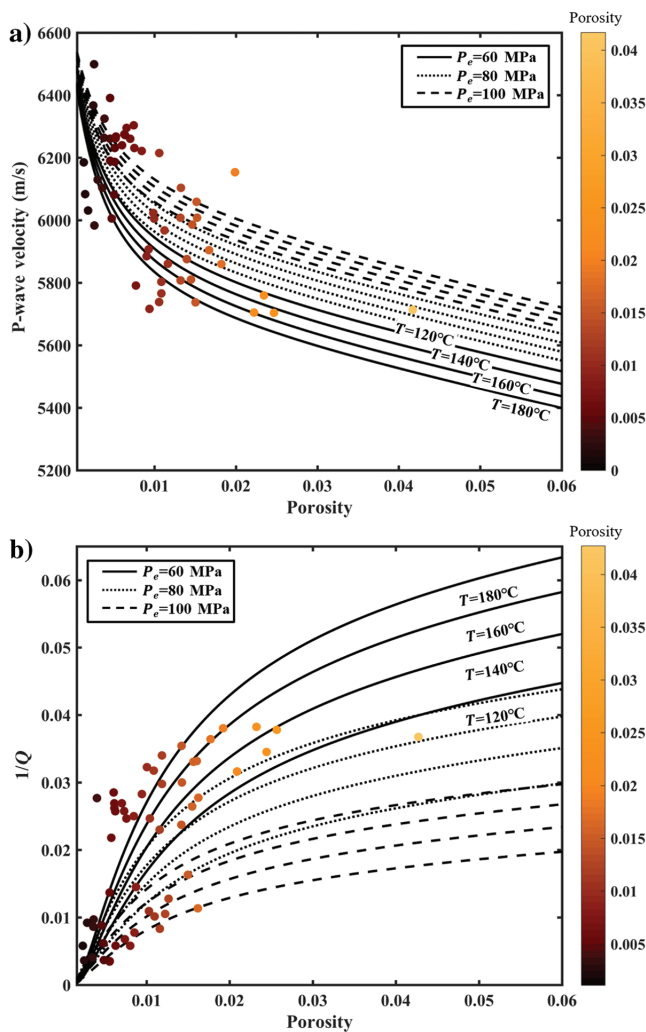


Figure 8. (a) The  $V_P$  and (b) dissipation factor as a function of porosity at seismic frequencies. The temperatures are given. The dashed, dotted, and solid lines correspond to differential pressures of 100, 80, and 60 MPa, respectively. The circles are the seismic data with different porosities (indicated by the color bar).

experimental  $V_P/V_S$ , P-wave impedance, and estimated attenuation by using the seismic data near the borehole (well B), with porosity ranging from 0 to 0.04, roughly corresponding to the porosity of the template. The data are within the calibrated template boundary, and the trend of the seismic porosity agrees with the theoretical curves, so that the template can be applied for the prediction of the TPP properties.

**PREDICTION OF TEMPERATURE, DIFFERENTIAL PRESSURE, AND POROSITY**

**Seismic inversion**

We invert the P-wave impedance and  $V_P/V_S$  ratio for a seismic line crossing three wells (A, B, and C), shown in Figure 12, in which the black line indicates the log porosity at well B. Porosity is closely related to the elastic properties; i.e., high porosity correlates with low P-wave impedance. However, in Figure 12b, the relationship between  $V_P/V_S$  and the porosity is not clear. Figure 13b shows the attenuation estimated with the improved frequency-shift method (Pang et al., 2019). The oil production reports at wells A, B,

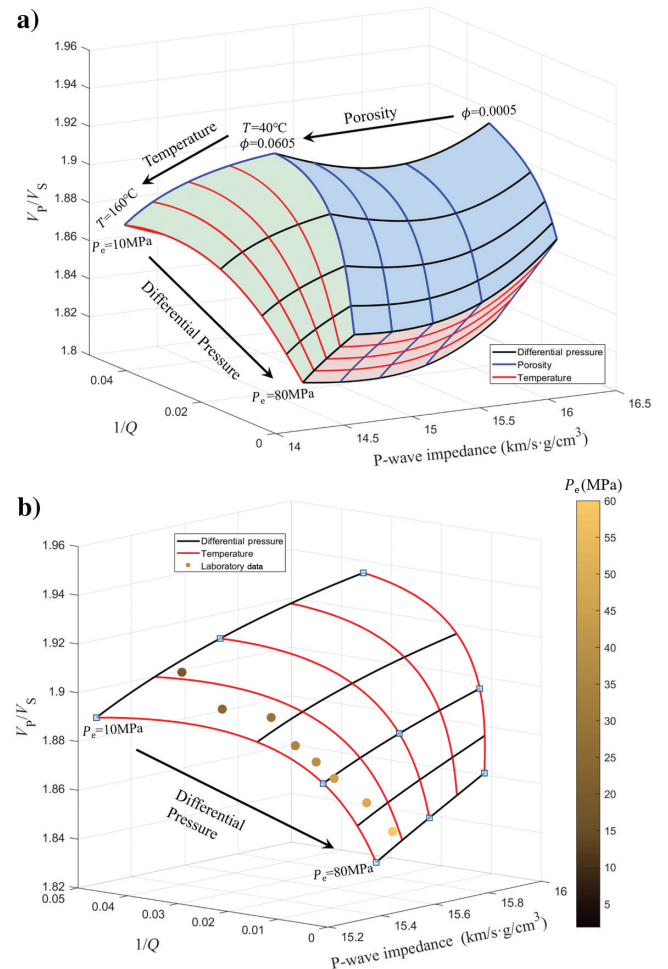


Figure 9. (a) The TPP-RPT at ultrasonic frequencies and (b) calibrated template with laboratory data (circles). The red and black lines correspond to isolines of temperature and differential pressure, respectively. The blue lines in (a) indicate isolines of porosity. The color bar indicates the differential pressure of the data.

Downloaded 03/25/22 to 222.195.191.131. Redistribution subject to SEG license or copyright; see Terms of Use at http://library.seg.org/page/policies/terms DOI: 10.1190/geo2020-0550.1

and C are 49.72, 90.26, and 50.31 tons per day, respectively. We can see that seismic attenuation decreases from well B to well A to well C, which is consistent with the reported values; i.e., high attenuation correlates with high oil production.

**Prediction**

The seismic data are superimposed on the template to predict the TPP properties, to obtain the distribution range of temperature, pressure, and porosity. The data symbols that lie outside the boundaries of the template do not correspond to typical carbonate rocks and are considered to be nonreservoir data (Ba et al., 2013). Figure 14 shows the TPP properties predicted by the template, showing that the temperature range is [125, 190]°C, the differential pressure range is [60, 100] MPa, and the porosity is less than 0.06. Compared with wells A and C, the more productive well B has the highest temperature and porosity and the lowest differential pressure. The predicted porosity at well B is in good agreement with the sonic

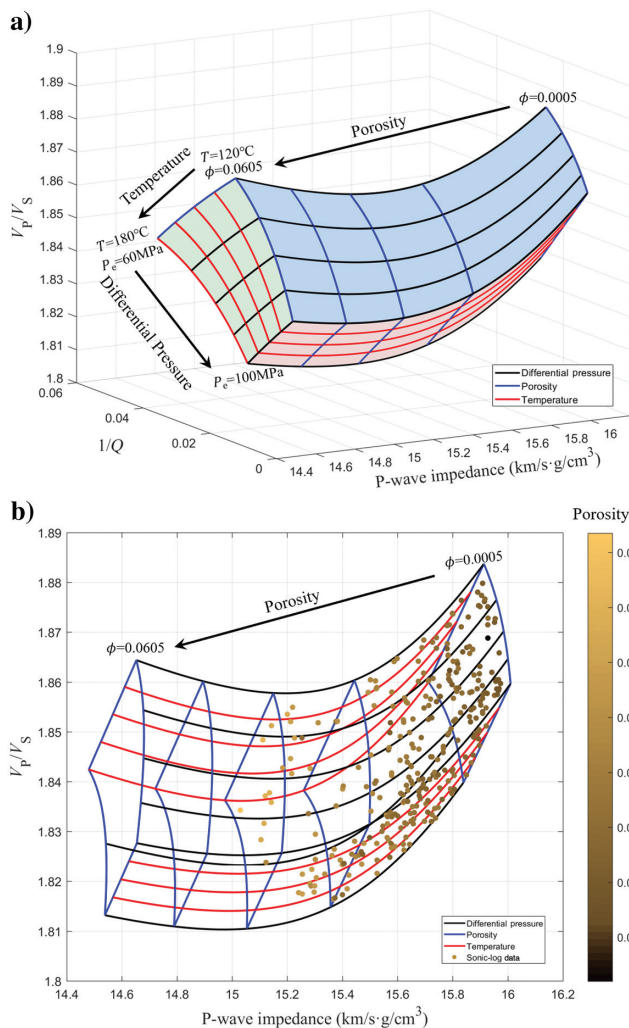


Figure 10. (a) The TPP-RPT at sonic frequencies and (b) calibrated template with sonic-log data (circles). The red, black, and blue lines correspond to isolines of temperature, differential pressure, and porosity, respectively. The color bar indicates the porosity of the data.

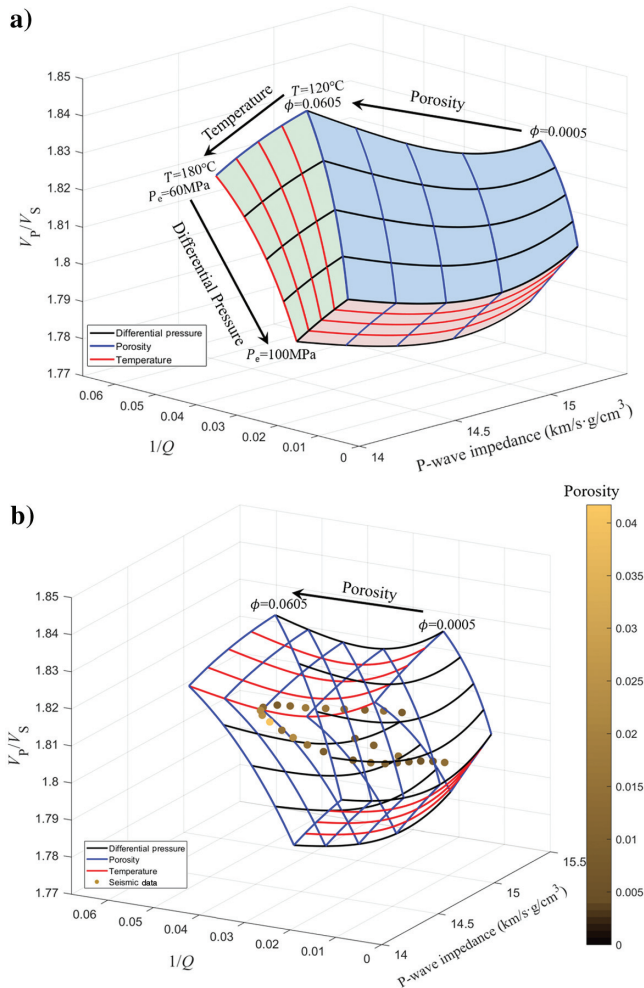


Figure 11. (a) The TPP-RPT at seismic frequencies and (b) calibrated template with the seismic data (circles). The red, black, and blue lines correspond to isolines of temperature, differential pressure, and porosity, respectively. The color bar indicates the porosity of the data.

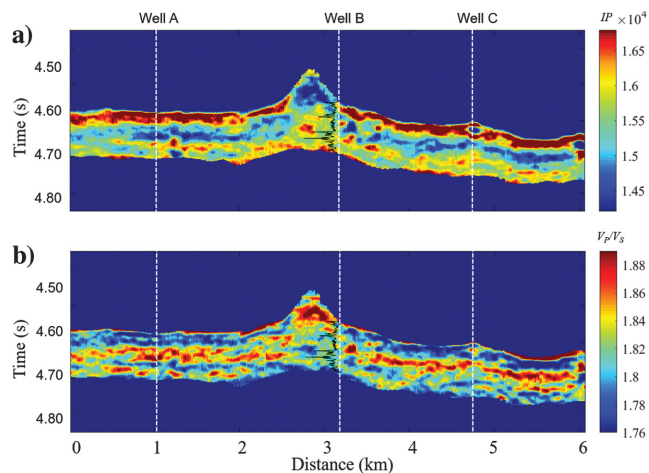


Figure 12. (a) The P-wave impedance and (b)  $V_p/V_s$  ratio profiles of the survey line crossing three wells (A, B, and C). The black line indicates the porosity of the log data at well B.

porosity (the black line in Figure 14c). Figure 15 shows the predicted porosity (the red line) and the log porosity (the black line). As can be appreciated, the trend is similar, which illustrates the reliability of the estimation process.

**Prediction of pore pressure**

The pore pressure  $P_p$  can be obtained from the principle of effective stress (Terzaghi, 1943),

$$P_p = P_0 - P_e, \tag{13}$$

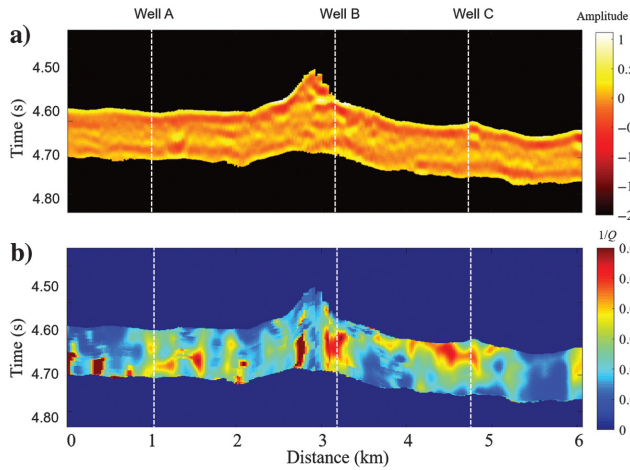


Figure 13. (a) Poststack seismic section and (b) seismic attenuation profiles of the survey line crossing three wells (A, B, and C).

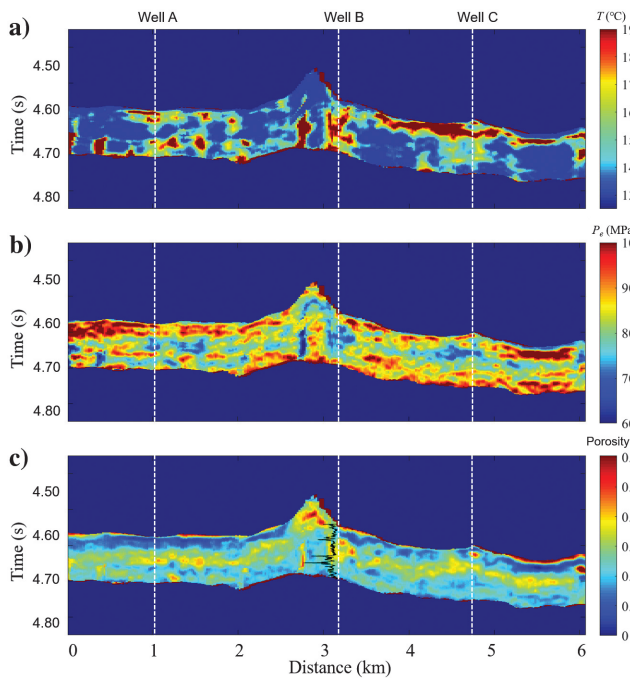


Figure 14. (a) Temperature, (b) differential pressure, and (c) porosity profiles of the survey line crossing three wells (A, B, and C). The black line indicates the porosity of the log data at well B.

where  $P_0$  and  $P_e$  are the confining and differential pressures, respectively. The confining pressure can be estimated by integrating the density log with depth (Carcione et al., 2003):

$$P_0 = \int_0^z \rho_z g dz, \tag{14}$$

where  $\rho_z$  is the density of the overburden at depth  $Z$  and  $g$  is the gravity constant.

Figure 16a and 16b shows the density and pore-pressure profiles of the seismic line crossing wells A, B, and C, respectively.

**Areal prediction**

Figure 17 shows an areal prediction with a surface of 56.25 km<sup>2</sup>. Well B has the highest temperature and porosity and the lowest differential pressure, whereas well A has the opposite situation. The inversion results are consistent with the actual oil productions,

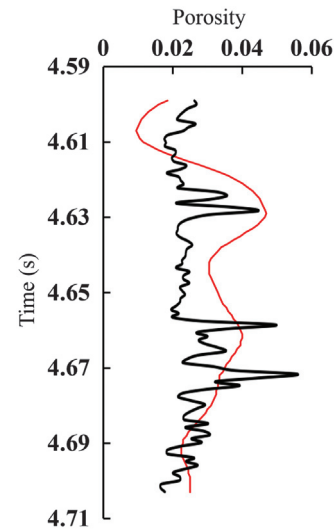


Figure 15. Predicted porosity (the red line) and log porosity (the black line).

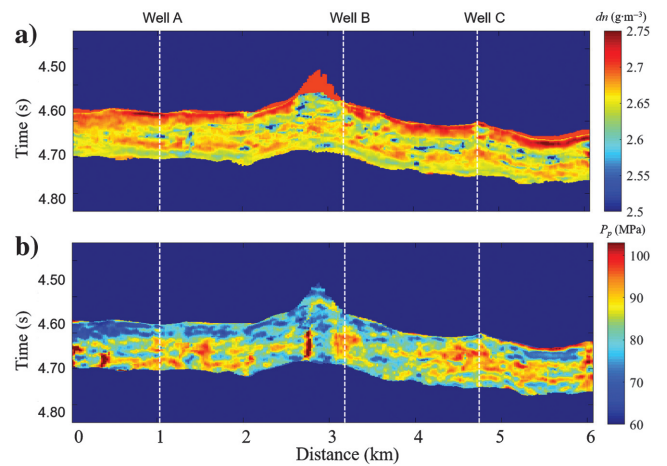


Figure 16. (a) Density and (b) pore pressure profiles of the survey line crossing three wells (A, B, and C).



and we have shown that the TPP properties can be estimated with confidence.

## DISCUSSION

The ultradeep Ordovician carbonate reservoirs in the S area of the Tarim Basin have complex TPP conditions and formation properties, and a proper exploitation of their hydrocarbon resources requires a quantitative estimation.

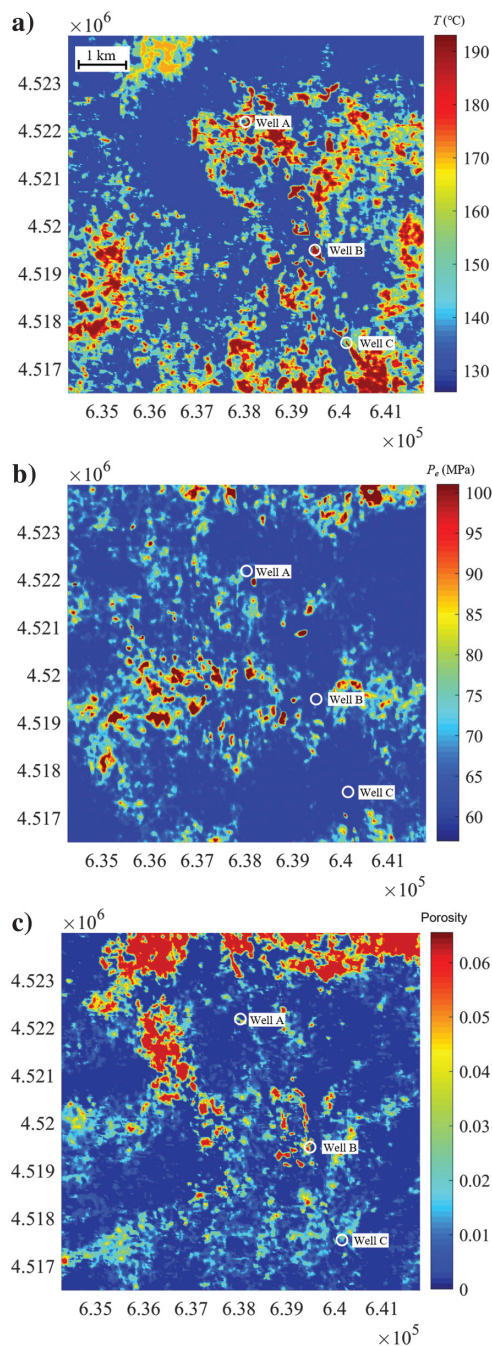


Figure 17. Areal prediction of (a) temperature, (b) differential pressure, and (c) porosity. The areal covers 56.25 km<sup>2</sup>, and the scale is given.

The temperature prediction in this work is somewhat uncertain because there is no well data to validate the results. The temperature range at 7 km in Liu et al. (2020) is 136°C–198°C for an area of approximately 35,000 km<sup>2</sup>, whereas in this work, we have 125°C–190°C on 56.25 km<sup>2</sup>, i.e., three orders of magnitude smaller than that of Liu et al. (2020), but the temperatures are similar. Liu et al. (2020) calculate the temperatures at depth based on assumptions about the thermal conductivity and shallow data, although with low resolution. On the contrary, we use higher resolution geophysical data, i.e., seismic data (wave velocity and attenuation), which reflect changes in the reservoir properties and lithology on a smaller scale. Uncertainties in the modeling process, seismic and instrumental noise, and multiple solutions of the inversion may lead to an apparent higher resolution, but the main trend should be reasonable, at least on an average basis.

As indicated by Davies and Smith (2006), hydrothermal dolomitization occurs under burial conditions of elevated temperature and pressure in the presence of fluids, whose temperature exceeds that of the host minerals (typically limestone) (Davies and Smith, 2006). Because the effect of temperature is assumed to be mainly caused by the fluid, the method provides higher values where fluids are present. Even if the porosity is relatively low, the reservoir has a good pore connectivity and this is the reason for patches of high temperature. Regions with poor connectivity show lower temperatures.

The attenuation-estimation error is a well-known problem in geophysical inversion, which, in this case, affects the temperature prediction. However, despite the uncertainties, the utility of well data to validate and calibrate the results is confirmed by the fact that the predictions are consistent with the actual oil production reports.

Further research is required to verify the heat-flow trends and temperature fields via numerical simulations and to collect relevant ultradeep reservoir temperature well data to constrain and validate the temperature field.

## CONCLUSION

We have developed a TPP rock-physics model to interpret ultradeep carbonate reservoirs, based on the Biot-Rayleigh theory. The model predicts the expected behavior of P-wave velocity and attenuation as a function of the above quantities, e.g., velocity and attenuation increase and decrease with differential pressure, and the effects of temperature are the opposite. Temperature has a significant effect on attenuation and differential pressure on  $V_P/V_S$  ratio, whereas porosity affects P-wave impedance. The  $V_P/V_S$  ratio first decreases and then increases with the increasing porosity.

Then, a multiscale 3D RPT is built, calibrated with laboratory, log, and seismic data to quantitatively obtain temperature, differential pressure, and porosity from seismic data. We consider three production wells of the S area in the Tarim Basin, China. Furthermore, we obtain profiles of the reservoir pore pressure from the differential pressure. We verify that the highest oil production is consistent with high temperature, low differential pressure, high porosity, and high pore pressure.

## ACKNOWLEDGMENTS

The authors are grateful for the support of the National Natural Science Foundation of China (grant nos. 41974123 and 41821002),

the Jiangsu Innovation and Entrepreneurship Plan and the Jiangsu Province Science Fund for Distinguished Young Scholars.

### DATA AND MATERIALS AVAILABILITY

Data associated with this research are available and can be obtained by contacting the corresponding author.

### APPENDIX A

#### SHAPE FACTORS $P$ AND $Q$

The terms  $P$  and  $Q$  are the shape factors related to the spheroidal aspect ratio  $\alpha_{\text{stiff}}$  and the Poisson's ratio  $\nu_0$  of the grains, given by (David and Zimmerman, 2012; Zhang et al., 2019)

$$P = \frac{(1 - \nu_s)}{6(1 - 2\nu_s)} \cdot \frac{4(1 + \nu_s) + 2\alpha^2(7 - 2\nu_s) - [3(1 + 4\nu_s) + 12\alpha^2(2 - \nu_s)]g}{2\alpha^2 + (1 - 4\alpha^2)g + (\alpha^2 - 1)(1 + \nu_s)g^2}, \quad (\text{A-1})$$

$$Q = \frac{4(\alpha^2 - 1)(1 - \nu_s)}{15\{8(\nu_s - 1) + 2\alpha^2(3 - 4\nu_s) + [(7 - 8\nu_s) - 4\alpha^2(1 - 2\nu_s)]g\}} \cdot \left\{ \frac{8(1 - \nu_s) + 2\alpha^2(3 + 4\nu_s) + [(8\nu_s - 1) - 4\alpha^2(5 + 2\nu_s)]g + 6(\alpha^2 - 1)(1 + \nu_s)g^2}{2\alpha^2 + (1 - 4\alpha^2)g + (\alpha^2 - 1)(1 + \nu_s)g^2} - 3 \left[ \frac{8(\nu_s - 1) + 2\alpha^2(5 - 4\nu_s) + [3(1 - 2\nu_s) + 6\alpha^2(\nu_s - 1)]g}{-2\alpha^2 + [(2 - \nu_s) + \alpha^2(1 + \nu_s)]g} \right] \right\}, \quad (\text{A-2})$$

where  $\nu_s = (3K_s - 2G_s)/(6K_s + 2G_s)$  and

$$g = \begin{cases} \frac{\alpha}{(1 - \alpha^2)^{3/2}} \left( \arccos \alpha - \alpha\sqrt{1 - \alpha^2} \right) & (\alpha < 1) \\ \frac{\alpha}{(1 - \alpha^2)^{3/2}} \left( \alpha\sqrt{1 - \alpha^2} - \operatorname{arccosh} \alpha \right) & (\alpha > 1) \end{cases}. \quad (\text{A-3})$$

### APPENDIX B

#### BATZLE AND WANG'S EQUATIONS

According to Batzle and Wang (1992), the density of oil  $\rho_f$  is

$$\rho_f = \frac{\rho_0 + (0.00277P - 1.71 \times 10^{-7}P^3)(\rho_0 - 1.15)^2 + 3.49 \times 10^{-4}P}{0.972 + 3.81 \times 10^{-4}(T + 17.78)^{1.175}}, \quad (\text{B-1})$$

where  $\rho_0$  is the reference density of petroleum, which is measured at the atmospheric pressure and 15.6°C.

The wave velocity of oil  $V_f$  is

$$V_f = 2096 \left( \frac{\rho_0}{2.6 - \rho_0} \right)^{0.5} - 3.7T + 4.64P + 0.0115[4.12(1.08\rho_0^{-1} - 1)^{0.5} - 1]TP. \quad (\text{B-2})$$

The modulus of oil  $k_f$  is

$$k_f = \rho_f \cdot V_f^2. \quad (\text{B-3})$$

The viscosity of oil  $\eta_f$  is

$$\eta_f = (10^{\wedge}[0.505 \times 10^{5.693 - 2.863/\rho_0} \times (17.8 + T)^{-1.163}] - 1) + 0.145P \times 10^{\wedge}[18.6 \times 0.1 \lg \eta_0 + (\lg \eta_0 + 2)^{-0.1} - 0.985], \quad (\text{B-4})$$

where  $\eta_0$  is the viscosity measured at the atmospheric pressure.

### APPENDIX C

#### ATTENUATION, DENSITY, AND STIFFNESS COEFFICIENTS

The dissipation coefficients of the two types of pores are

$$b_i = \frac{\eta \phi_i^2}{\kappa_i}, \quad i = 1, 2. \quad (\text{C-1})$$

The density components of the dual-pore medium are

$$\begin{aligned} \rho_{11} &= (1 - \phi_1 - \phi_2)\rho_s + \frac{1}{2}(2 - \phi_1 - \phi_2)\rho_f, \\ \rho_{12} &= \frac{1}{2}(\phi_1 - 1)\rho_f, \\ \rho_{13} &= \frac{1}{2}(\phi_2 - 1)\rho_f, \\ \rho_{22} &= \frac{1}{2}(\phi_1 + 1)\rho_f, \\ \rho_{33} &= \frac{1}{2}(\phi_2 + 1)\rho_f, \end{aligned} \quad (\text{C-2})$$

where  $\rho_s$  and  $\rho_f$  are the grain and fluid densities, respectively.

The stiffness coefficients are

$$\begin{aligned} \beta &= \frac{\zeta^{(1)}}{\zeta^{(2)}}, \\ N &= G_b, \\ Q_1 &= \frac{\beta(1 - \phi_1 - \phi_2 - K_b/K_s)\phi_1 K_s}{\beta(1 - \phi_1 - \phi_2 - K_b/K_s) + K_s/K_f(\beta\phi_1 + \phi_2)}, \\ Q_2 &= \frac{(1 - \phi_1 - \phi_2 - K_b/K_s)\phi_2 K_s}{1 - \phi_1 - \phi_2 - K_b/K_s + K_s/K_f(\beta\phi_1 + \phi_2)}, \\ R_1 &= \frac{(\beta\phi_1 + \phi_2)\phi_1 K_s}{\beta(1 - \phi_1 - \phi_2 - K_b/K_s) + K_s/K_f(\beta\phi_1 + \phi_2)}, \\ R_2 &= \frac{(\beta\phi_1 + \phi_2)\phi_2 K_s}{1 - \phi_1 - \phi_2 - K_b/K_s + K_s/K_f(\beta\phi_1 + \phi_2)}, \\ A &= (1 - \phi)K_s - \frac{2}{3}N - (Q_1 + Q_2)K_s/K_f, \end{aligned} \quad (\text{C-3})$$

where  $K_s$  and  $K_f$  are the grain and fluid bulk moduli, respectively. The dry-rock modulus  $K_b$  and  $G_b$  can be obtained from the equivalent moduli  $K_{\text{eff}}$  and  $G_{\text{eff}}$  of the effective-medium theory.

## APPENDIX D

## DISPERSION EQUATION

Substituting a plane P-wave kernel  $e^{i(\omega t - k \cdot x)}$  into equation 11 yields

$$\begin{vmatrix} a_{11}k^2 + b_{11} & a_{12}k^2 + b_{12} & a_{13}k^2 + b_{13} \\ a_{21}k^2 + b_{21} & a_{22}k^2 + b_{22} & a_{23}k^2 + b_{23} \\ a_{31}k^2 + b_{31} & a_{32}k^2 + b_{32} & a_{33}k^2 + b_{33} \end{vmatrix} = 0, \quad (\text{D-1})$$

where  $\omega$  is the angular frequency and  $k$  is the complex wavenumber. Moreover,

$$\begin{aligned} a_{11} &= A + 2N + i(Q_2\phi_1 - Q_1\phi_2)x_1, & b_{11} &= -\rho_{11}\omega^2 + i\omega(b_1 + b_2), \\ a_{12} &= Q_1 + i(Q_2\phi_1 - Q_1\phi_2)x_1, & b_{12} &= -\rho_{12}\omega^2 - i\omega b_1, \\ a_{13} &= Q_2 + i(Q_2\phi_1 - Q_1\phi_2)x_3, & b_{13} &= -\rho_{13}\omega^2 - i\omega b_2, \\ a_{21} &= Q_1 - iR_1\phi_2x_1, & b_{21} &= -\rho_{12}\omega^2 - i\omega b_1, \\ a_{22} &= R_1 - iR_1\phi_2x_2, & b_{22} &= -\rho_{22}\omega^2 + i\omega b_1, \\ a_{23} &= -iR_1\phi_2x_3, & b_{23} &= 0, \\ a_{31} &= Q_2 + iR_2\phi_1x_1, & b_{31} &= -\rho_{13}\omega^2 - i\omega b_2, \\ a_{32} &= iR_2\phi_1x_2, & b_{32} &= 0, \\ a_{33} &= R_2 + iR_2\phi_1x_3, & b_{33} &= -\rho_{33}\omega^2 + i\omega b_2, \end{aligned} \quad (\text{D-2})$$

where

$$\begin{aligned} x_1 &= i(\phi_2Q_1 - \phi_1Q_2)/Z, & x_2 &= i\phi_2R_1/Z, & x_3 &= -i\phi_1R_2/Z, \\ Z &= \frac{i\omega\eta\phi_1^2\phi_2\phi_{20}R_0^2}{3\kappa_{10}} - \frac{\rho_f\omega^2R_0^2\phi_1^2\phi_2\phi_{20}}{3\phi_{10}} - (\phi_2^2R_1 + \phi_1^2R_2). \end{aligned} \quad (\text{D-3})$$

## REFERENCES

- Agersborg, R., T. A. Johansen, and M. Jakobsen, 2009, Velocity variations in carbonate rocks due to dual porosity and wave-induced fluid flow: *Geophysical Prospecting*, **57**, 81–98, doi: [10.1111/j.1365-2478.2008.00733.x](https://doi.org/10.1111/j.1365-2478.2008.00733.x).
- Aki, K., and P. G. Richards, 1980, *Quantitative seismology: Theory and methods*: W.H. Freeman and Company.
- Ba, J., H. Cao, J. M. Carcione, G. Tang, X. Yan, W. Sun, and J. Nie, 2013, Multiscale rock-physics templates for gas detection in carbonate reservoirs: *Journal of Applied Geophysics*, **93**, 77–82, doi: [10.1016/j.jappgeo.2013.03.011](https://doi.org/10.1016/j.jappgeo.2013.03.011).
- Ba, J., J. M. Carcione, H. Cao, Q. Z. Du, Z. Y. Yuan, and M. H. Lu, 2012, Velocity dispersion and attenuation of P waves in partially-saturated rocks: Wave propagation equations in double-porosity medium: *Chinese Journal of Geophysics*, **55**, 219–231, doi: [10.6038/j.issn.0001-5733.2012.01.021](https://doi.org/10.6038/j.issn.0001-5733.2012.01.021).
- Ba, J., J. M. Carcione, and J. X. Nie, 2011, Biot-Rayleigh theory of wave propagation in double-porosity media: *Journal of Geophysical Research*, *Solid Earth*, **116**, B06202, doi: [10.1029/2010JB008185](https://doi.org/10.1029/2010JB008185).
- Ba, J., W. H. Xu, L.-Y. Fu, J. M. Carcione, and L. Zhang, 2017, Rock anelasticity due to patchy saturation and fabric heterogeneity: A double double-porosity model of wave propagation: *Journal of Geophysical Research*, *Solid Earth*, **122**, 1949–1976, doi: [10.1002/2016JB013882](https://doi.org/10.1002/2016JB013882).
- Batzle, M. L., D.-H. Han, and R. Hofmann, 2006, Fluid mobility and frequency-dependent seismic velocity — Direct measurements: *Geophysics*, **71**, no. 1, N1–N9, doi: [10.1190/1.2159053](https://doi.org/10.1190/1.2159053).
- Batzle, M. L., and Z. Wang, 1992, Seismic properties of pore fluids: *Geophysics*, **57**, 1396–1408, doi: [10.1190/1.1443207](https://doi.org/10.1190/1.1443207).
- Biot, M. A., 1962, Mechanics of deformation and acoustic propagation in porous media: *Journal of Applied Physics*, **33**, 1482–1498, doi: [10.1063/1.1728759](https://doi.org/10.1063/1.1728759).
- Carcione, J. M., H. B. Helle, N. H. Pham, and T. Toverud, 2003, Pore pressure estimation in reservoir rocks from seismic reflection data: *Geophysics*, **68**, 1569–1579, doi: [10.1190/1.1620631](https://doi.org/10.1190/1.1620631).
- Chapman, S., B. Quintal, N. Tisato, and K. Holliger, 2017, Frequency scaling of seismic attenuation in rocks saturated with two fluid phases: *Geophysical Journal International*, **208**, 221–225, doi: [10.1093/gji/ggw387](https://doi.org/10.1093/gji/ggw387).
- Chapman, S., N. Tisato, B. Quintal, and K. Holliger, 2016, Seismic attenuation in partially saturated Berea sandstone submitted to a range of confining pressures: *Journal of Geophysical Research*, *Solid Earth*, **121**, 1664–1676, doi: [10.1002/2015JB012575](https://doi.org/10.1002/2015JB012575).
- Cheng, C. H., and M. N. Toksöz, 1979, Inversion of seismic velocities for the pore aspect ratio spectrum of a rock: *Journal of Geophysical Research*, *Solid Earth*, **84**, 7533–7543, doi: [10.1029/JB084iB13p07533](https://doi.org/10.1029/JB084iB13p07533).
- Cheng, W., J. M. Carcione, A. Qadrouh, M. Alajmi, and J. Ba, 2020, Rock anelasticity, pore geometry and the Biot-Gardner effect: *Rock Mechanics and Rock Engineering*, **53**, 3969–3981, doi: [10.1007/s00603-020-02155-7](https://doi.org/10.1007/s00603-020-02155-7).
- Cheng, Y. F., X. Shi, L. Li, L. Y. Wu, and W. Mei, 2013, A novel pore pressure prediction model of carbonate formation with fracture development: *Journal of China University of Petroleum*, **37**, 83–97, doi: [10.3969/j.issn.1673-5005.2013.03.014](https://doi.org/10.3969/j.issn.1673-5005.2013.03.014).
- David, E. C., and R. W. Zimmerman, 2012, Pore structure model for elastic wave velocities in fluid-saturated sandstones: *Journal of Geophysical Research*, *Solid Earth*, **117**, B07210, doi: [10.1029/2012JB009195](https://doi.org/10.1029/2012JB009195).
- Davies, G. R., and L. B. Smith, 2006, Structurally controlled hydrothermal dolomite reservoir facies: An overview: *AAPG Bulletin*, **90**, 1641–1690, doi: [10.1306/05220605164](https://doi.org/10.1306/05220605164).
- Ding, Z. W., R. J. Wang, F. F. Chen, J. P. Yang, Z. Q. Zhu, Z. M. Yang, X. H. Sun, B. Xian, E. P. Li, T. Shi, C. Zuo, and Y. Li, 2020, Origin, hydrocarbon accumulation and oil-gas enrichment of fault-karst carbonate reservoirs: A case study of Ordovician carbonate reservoirs in South Tahe area of Halahtang oilfield, Tarim Basin: *Petroleum Exploration and Development*, **47**, 306–317, doi: [10.1016/S1876-3804\(20\)60048-9](https://doi.org/10.1016/S1876-3804(20)60048-9).
- Duran, E. L., L. Adam, I. C. Wallis, and A. Barnhoorn, 2019, Mineral alteration and fracture influence on the elastic properties of volcanoclastic rocks: *Journal of Geophysical Research*, *Solid Earth*, **124**, 4576–4600, doi: [10.1029/2018JB016617](https://doi.org/10.1029/2018JB016617).
- Eaton, A., 1972, Graphical method predicts geopressures worldwide: *World Oil*, **183**, 51–56.
- Fillippone, R., 1979, On the prediction of abnormally pressured sedimentary rocks from seismic data: *Offshore Technology Conference*, 2667–2676.
- Gassmann, F., 1951, Elasticity of porous media: *Vierteljahrsschrift der Naturforschenden Gesellschaft*, **96**, 1–23.
- Gregory, A. R., 1976, Fluid saturation effects on dynamic elastic properties of sedimentary rocks: *Geophysics*, **41**, 895–921, doi: [10.1190/1.1440671](https://doi.org/10.1190/1.1440671).
- Gu, Y., Y. L. Wan, J. W. Huang, X. B. Zhuang, B. Wang, and M. Li, 2019, Prospects for ultra-deep oil and gas in the “deep burial and high pressure” Tarim Basin: *Petroleum Geology & Experiment*, **41**, 157–164.
- Guo, M., L.-Y. Fu, and J. Ba, 2009, Comparison of stress-associated coda attenuation and intrinsic attenuation from ultrasonic measurements: *Geophysical Journal International*, **178**, 447–456, doi: [10.1111/j.1365-246X.2009.04159.x](https://doi.org/10.1111/j.1365-246X.2009.04159.x).
- Guo, X. S., D. F. Hu, Y. P. Li, J. B. Duan, X. F. Zhang, X. J. Fan, H. Duan, and W. C. Li, 2019, Theoretical progress and key technologies of onshore ultra-deep oil/gas exploration: *Engineering*, **5**, 458–470, doi: [10.1016/j.eng.2019.01.012](https://doi.org/10.1016/j.eng.2019.01.012).
- Hill, R., 1952, The elastic behaviour of a crystalline aggregate: *Proceedings of the Physical Society*, **65**, 349–354, doi: [10.1088/0370-1298/65/5/307](https://doi.org/10.1088/0370-1298/65/5/307).
- Hottman, E., and K. Johnson, 1965, Estimation of formation pressures from log-derived shale properties: *Journal of Petroleum Technology*, **17**, 717–722, doi: [10.2118/1110-PA](https://doi.org/10.2118/1110-PA).
- Jaya, M. S., S. A. Shapiro, L. H. Kristinsdóttir, D. Bruhnc, H. Milsch, and E. Spangenberg, 2010, Temperature dependence of seismic properties in geothermal rocks at reservoir conditions: *Geothermics*, **39**, 115–123, doi: [10.1016/j.geothermics.2009.12.002](https://doi.org/10.1016/j.geothermics.2009.12.002).
- Jiao, F. Z., 2018, Significance and prospect of ultra-deep carbonate fault-karst reservoirs in Shunbei area, Tarim Basin: *Oil & Gas Geology*, **39**, 207–216, doi: [10.11743/ogg20180201](https://doi.org/10.11743/ogg20180201).
- Kern, H., T. Popp, F. Gorbatsevich, A. Zharikov, K. V. Lobanov, and Y. P. Smirnov, 2001, Pressure and temperature dependence of  $V_P$  and  $V_S$  in rocks from the superdeep well and from surface analogues at Kola and the nature of velocity anisotropy: *Tectonophysics*, **338**, 113–134, doi: [10.1016/S0040-1951\(01\)00128-7](https://doi.org/10.1016/S0040-1951(01)00128-7).
- Kuster, G. T., and M. N. Toksöz, 1974, Velocity and attenuation of seismic waves in two-phase media — Part I: Theoretical formulations: *Geophysics*, **39**, 587–606, doi: [10.1190/1.1440450](https://doi.org/10.1190/1.1440450).
- Lei, J., B. Pan, Y. Guo, Y. Fan, Y. Xu, and N. Zou, 2020, The temperature distribution model and its application to reservoir depth prediction in fault-karst carbonate reservoirs: *Arabian Journal of Geosciences*, **13**, 1–11, doi: [10.1007/s12517-020-05696-x](https://doi.org/10.1007/s12517-020-05696-x).
- Li, H. B., J. J. Zhang, S. J. Cai, and H. J. Pan, 2019, 3D rock physics template for reservoirs with complex pore structure: *Chinese Journal of Geophysics*, **62**, 2711–2723.



- Liu, B., H. Kern, and T. Popp, 1998, Velocities and attenuation of P- and S-waves in dry and wet rocks with different porosities under different confining pressures: *Chinese Journal of Geophysics*, **41**, 537–546.
- Liu, Y. C., N. S. Qiu, H. L. Li, A. L. Ma, J. Chang, and J. K. Jia, 2020, Terrestrial heat flow and crustal thermal structure in the northern slope of Tazhong uplift in Tarim Basin: *Geothermics*, **83**, 101709, doi: [10.1016/j.geothermics.2019.101709](https://doi.org/10.1016/j.geothermics.2019.101709).
- Mavko, G., T. Mukerji, and J. Dvorkin, 2009, *The rock physics handbook: Tools for seismic analysis in porous media*: Cambridge University Press.
- Mori, T., and K. Tanaka, 1973, Average stress in matrix and average elastic energy of materials with misfitting inclusions: *Acta Metallurgica*, **21**, 571–574, doi: [10.1016/0001-6160\(73\)90064-3](https://doi.org/10.1016/0001-6160(73)90064-3).
- Murphy, W. F., 1984, Acoustic measures of partial gas saturation in tight sandstones: *Journal of Geophysical Research, Solid Earth*, **89**, 11549–11559, doi: [10.1029/JB089iB13p11549](https://doi.org/10.1029/JB089iB13p11549).
- Odegaard, E., and P. A. Avseth, 2004, Well log and seismic data analysis using rock physics templates: *First Break*, **22**, 37–43, doi: [10.3997/1365-2397.2004017](https://doi.org/10.3997/1365-2397.2004017).
- Pang, M. Q., J. Ba, J. M. Carcione, S. Picotti, J. Zhou, and R. Jiang, 2019, Estimation of porosity and fluid saturation in carbonates from rock-physics templates based on seismic Q: *Geophysics*, **84**, no. 6, M25–M36, doi: [10.1190/geo2019-0031.1](https://doi.org/10.1190/geo2019-0031.1).
- Pang, M. Q., J. Ba, J. M. Carcione, A. Vesnaver, R. P. Ma, and T. S. Chen, 2020, Analysis of attenuation rock-physics template of tight sandstones: Reservoir microcrack prediction: *Chinese Journal of Geophysics*, **63**, 4205–4219.
- Pang, X. Q., C. Z. Jia, and W. Y. Wang, 2015, Petroleum geology features and research developments of hydrocarbon accumulation in deep petroliferous basins: *Petroleum Science*, **12**, 1–53, doi: [10.1007/s12182-015-0014-0](https://doi.org/10.1007/s12182-015-0014-0).
- Pham, N. H., J. M. Carcione, H. B. Helle, and B. Ursin, 2008, Wave velocities and attenuation of shaley sandstones as a function of pore pressure and partial saturation: *Geophysical Prospecting*, **50**, 615–627, doi: [10.1046/j.1365-2478.2002.00343.x](https://doi.org/10.1046/j.1365-2478.2002.00343.x).
- Pimienta, L., J. Fortin, and Y. Guéguen, 2015, Experimental study of Young's modulus dispersion and attenuation in fully saturated sandstones: *Geophysics*, **80**, no. 5, L57–L72, doi: [10.1190/geo2014-0532.1](https://doi.org/10.1190/geo2014-0532.1).
- Pimienta, L., J. Fortin, and Y. Guéguen, 2016, Effect of fluids and frequencies on Poisson's ratio of sandstone samples: *Geophysics*, **81**, no. 2, D183–D195, doi: [10.1190/geo2015-0310.1](https://doi.org/10.1190/geo2015-0310.1).
- Pride, S. R., J. G. Berryman, and J. M. Harris, 2004, Seismic attenuation due to wave induced flow: *Journal of Geophysical Research*, **109**, B01201, doi: [10.1029/2003JB002639](https://doi.org/10.1029/2003JB002639).
- Qi, L. X., 2016, Oil and gas breakthrough in ultra-deep Ordovician carbonate formations in Shuntuoguole uplift, Tarim Basin: *China Petroleum Exploration*, **21**, 38–51.
- Quan, Y. L., and J. M. Harris, 1997, Seismic attenuation tomography using the frequency shift method: *Geophysics*, **62**, 895–905, doi: [10.1190/1.1444197](https://doi.org/10.1190/1.1444197).
- Reuss, A., 1929, Calculation of the flow limits of mixed crystals on the basis of the plasticity of monocrystals: *Zeitschrift für Angewandte Mathematik und Mechanik*, **9**, 49–58, doi: [10.1002/zamm.19290090104](https://doi.org/10.1002/zamm.19290090104).
- Ruiz, F., and A. Cheng, 2010, A rock physics model for tight gas sand: *The Leading Edge*, **29**, 1484–1489, doi: [10.1190/1.3525364](https://doi.org/10.1190/1.3525364).
- Sarout, J., E. Cazes, C. D. Plane, A. Arena, and L. Esteban, 2017, Stress-dependent permeability and wave dispersion in tight cracked rocks: Experimental validation of simple effective medium models: *Journal of Geophysical Research, Solid Earth*, **122**, 6180–6201, doi: [10.1002/2017JB014147](https://doi.org/10.1002/2017JB014147).
- Smith, T., C. Sondergeld, and A. O. Tinni, 2010, Microstructural controls on electric and acoustic properties in tight gas sandstones: some empirical data and observations: *The Leading Edge*, **29**, 1470–1474, doi: [10.1190/1.3525362](https://doi.org/10.1190/1.3525362).
- Terzaghi, K., 1943, *Theoretical soil mechanics*: John Wiley & Sons.
- Tian, F., Q. Y. Di, Q. Jin, F. Q. Cheng, W. Zhang, L. M. Lin, Y. Wang, D. B. Yang, C. K. Niu, and Y. X. Li, 2019, Multiscale geological-geophysical characterization of the epigenic origin and deeply buried paleokarst system in Tahe Oilfield, Tarim Basin: *Marine and Petroleum Geology*, **102**, 16–32, doi: [10.1016/j.marpetgeo.2018.12.029](https://doi.org/10.1016/j.marpetgeo.2018.12.029).
- Toksöz, M. N., H. D. Johnston, and A. Timur, 1979, Attenuation of seismic waves in dry and saturated rocks — I: Laboratory measurements: *Geophysics*, **44**, 681–690, doi: [10.1190/1.1440969](https://doi.org/10.1190/1.1440969).
- Tran, D. T., C. S. Rai, and C. H. Sondergeld, 2008, Changes in crack aspect-ratio concentration from heat treatment: A comparison between velocity inversion and experimental data: *Geophysics*, **73**, no. 4, E123–E132, doi: [10.1190/1.2928848](https://doi.org/10.1190/1.2928848).
- Tu, N., and W. Lu, 2009, An improved peak-frequency-shift method for Q estimation: CPS/SEG Beijing 2009 International Geophysical Conference & Exposition.
- Voigt, W., 1910, *Lehrbuch der Kristallphysik*: Teubner.
- Walsh, J., 1965, The effect of cracks on the compressibility of rock: *Journal of Geophysical Research*, **70**, 381–389, doi: [10.1029/JZ070i002p00381](https://doi.org/10.1029/JZ070i002p00381).
- Wan, Y. L., Y. Gu, Q. Fu, X. B. Zhuang, Z. B. Shao, and Y. Ding, 2017, Characteristics of geothermal-geopressure field and its implications for the process of hydrocarbon distribution in deep ordovician stratum in Shunnan-Gulong area of Tarim Basin: *Mineralogy and Petrology*, **37**, 74–78.
- Wei, Y. J., J. Ba, R. P. Ma, L. Zhang, J. M. Carcione, and M. Q. Guo, 2020, Effect of effective pressure change on pore structure and elastic wave responses in tight sandstones: *Chinese Journal of Geophysics*, **63**, 2810–2822.
- Xia, H. Q., X. B. You, Z. Lin, and Y. B. Song, 2005, Logging calculation for pore pressure on carbonate rock formation based on effective stress method: *Drilling & Production Technology*, **3**, 28–30.
- Yao, J., Z. Q. Huang, W. Z. Liu, Y. Zhang, Q. D. Zeng, and X. Yan, 2018, Key mechanical problems in the development of deep oil and gas reservoirs: *Scientia Sinica Physica, Mechanica & Astronomica*, **48**, 044701.
- Zhang, C. J., and T. J. Ulrych, 2002, Estimation of quality factors from CMP records: *Geophysics*, **67**, 1542–1547, doi: [10.1190/1.1512799](https://doi.org/10.1190/1.1512799).
- Zhang, L., J. Ba, L.-Y. Fu, J. M. Carcione, and C. Cao, 2019, Estimation of pore microstructure by using the static and dynamic moduli: *International Journal of Rock Mechanics and Mining Sciences*, **113**, 24–30, doi: [10.1016/j.ijrmms.2018.11.005](https://doi.org/10.1016/j.ijrmms.2018.11.005).
- Zimmerman, R. W., 1991, *Compressibility of sandstones*: Elsevier.

Biographies and photographs of the authors are not available.